Chemical Physics 175 (1993) 99–111
North-Holland

Population distributions in the vibrational deactivation of benzene and benzene-d_6. First and second moments derived from two-color infrared fluorescence measurements

Jerrell D. Brenner, Joseph P. Erinjeri and John R. Barker

Department of Chemistry and Department of Atmospheric, Oceanic, and Space Sciences, Space Physics Research Laboratory, The University of Michigan, Ann Arbor, MI 48109-2143, USA

Received 19 March 1993

Time-resolved two-color infrared fluorescence (IRF) from highly vibrationally excited benzene and benzene-d_6 has been used to determine means and variances of the excited molecule population distributions over the majority of the energy range during deactivation via collisional energy transfer to unexcited molecules. These measurements extend the IRF technique to produce information about the first two moments of energy transfer induced population distributions present during the collisional deactivation process. A simple means of analysis of IRF from multiple emission bands is presented, which in principle yields information about higher moments, as well as increasingly precise determination of lower moments. Results from this analysis are independent of any assumed models for collisional energy transfer. In the experiments, simultaneous monitoring of IRF from the C–H (C–D) stretching mode fundamental region at ≈ 3060 cm^{-1} (≈ 2290 cm^{-1}) and first overtone region at ≈ 6000 cm^{-1} (≈ 4500 cm^{-1}), allows independent observation of two subsets of the total population of excited molecules, each containing the vibrational energy required to emit photons in the observed bands. Similar results are obtained from analysis of the time- and wavelength-resolved $\Delta v = -1$ C–H stretch emission spectrum of highly excited benzene-h_6 as it is deactivated by collisions. The two-color results are shown to provide meaningful information about the first two moments of the energy population distribution over much of the energy range. Knowledge of the population distribution is important since it results directly from the form of $P_c(E', E)$, the step size probability distribution function for collisional energy transfer. Master equation simulations are used together with these results in order to derive some limitations on the possible forms of $P_c(E', E)$.

1. Introduction

Several experimental techniques have been developed in order to measure fundamental energy transfer properties in vibrationally excited electronic ground state polyatomic molecules. (For reviews, see refs. [1–3].) These techniques rely on relating a physical observable, such as infrared emission or UV absorption, to the average energy of the excited species as it is deactivated by collisions. In most of these studies, laser excitation followed by radiationless transitions produces a population of highly vibrationally excited molecules with a narrow initial distribution of energies, which presumably broadens as the molecules are deactivated. The deactivation is subject to an unknown energy transfer step size probability distribution function $P_c(E', E)$, which describes the probability that an excited molecule with energy E prior to a collision will have energy E' following the collision. Since the experimental techniques as first developed were only sensitive to properties averaged over the excited molecule energy distribution (such as $\langle\langle \Delta E \rangle\rangle$, the average energy transferred per collision), little information existed regarding the form of $P_c(E', E)$. In the absence of detailed information, simple, empirical forms for $P_c(E', E)$ were adopted in models of systems where collisional energy transfer is important, such as unimolecular reaction and chemical activation studies [3–5].

More recently, some experimental techniques have achieved access to the excited molecule energy population distribution, and thus $P_c(E', E)$. A very promising approach [6–8] uses multiphoton ionization to monitor the time following excitation when the excited molecules are deactivated into a narrow

energy range at lower energy. This technique yields a detailed picture of the distribution of arrival times to the energy window; however, in experiments to date only energy windows in the lowest 10 percent or so of available energies have been accessible, so that the population distribution at higher energies must be inferred with the aid of master equation models and simulations. A second technique [9,10] measures the fraction of collisions which transfer sufficient energy to induce isomerization in a collider molecule, yielding some information about the large step size tail of $P_c(E', E)$ for the collision pairs under study. Finally, a recently developed total fluorescence technique [11] has been used to derive information about $P_c(E', E)$ in the deactivation of excited NO_2.

In this paper, an extension of the IRF technique is described which is capable of producing information about higher moments of the excited molecule energy population distributions, and yields some information about the functional form of $P_c(E', E)$. The major advantage of this method over experiments previously described is that it is possible to determine moments of the distribution at almost all energies, rather than just a narrow range of energies or a small portion of the distribution. Furthermore, the results are independent of any assumed models for $P_c(E', E)$. In the two-color IRF experiments described here, the energy range is limited at high energies by slow detector response and at low energies by low S/N and insensitivity to the portion of the population distribution with energies below the upper level of the observed IRF transitions. In principle, these limitations can be overcome by using faster, more sensitive detectors and observing lower energy bands. In addition, as described below, observation of multiple bands can provide information about the third and higher moments of the population distribution as well as more precise measurement of the lower moments. Such experiments on benzene and other molecules are planned in the near future.

The two-color technique involves simultaneous monitoring of IRF from widely separated bands (e.g. the C–H stretch fundamental and first overtone), such that the excited molecules emitting in each band comprise well-defined subsets of the energy population distribution. Emission intensities of the two bands are related to the vibrational energy content of the emitting molecule by a well-tested theoretical expression (see discussion in ref. [1]), and the relative intensities are quite sensitive to the width of the population distribution. In previous IRF studies of energy transfer (e.g. refs. [12,13]), $\langle\langle \Delta E \rangle\rangle$ has been determined as a function of $\langle\langle E_{vib} \rangle\rangle$ by assuming the distribution to be narrow (i.e., microcanonical) throughout the decay, and the effects on $\langle\langle \Delta E \rangle\rangle$ of varying the shape of the distribution were investigated using master equation simulations involving assumed forms for $P_c(E', E)$. In the present study, similar master equation simulations are used in order to place limits on the form of $P_c(E', E)$, but the first and second moments deduced from the experiment are independent of any assumed forms for $P_c(E', E)$.

2. Experimental

The basic method of the IRF technique has been thoroughly described [1,12–14]. In the present experiments, a KrF excimer laser at 248 nm irradiated pure gas-phase benzene or benzene-d_6 in a 35 cm long $\times$ 3.2 cm diameter pyrex cell fitted with two sapphire side windows for transmitting infrared radiation. Following absorption of the UV light, fast radiationless processes in both benzene and benzene-d_6 produce highly vibrationally excited ($\approx$40700 and 40900 cm^{-1}, respectively) ground state species within about one microsecond (see refs. [12] and [14], respectively, for details of relevant benzene-h_6 and benzene-d_6 photophysics). Subsequent infrared emission from the excited molecules was monitored using two 77 K InSb infrared detectors (Infrared Associates), looking through opposing side windows. For the benzene-h_6 experiments, emission from the C–H stretch region at $\approx$3000 cm^{-1} was isolated using a bandpass filter which transmitted frequencies between 2000 and 3300 cm^{-1}. The opposing detector monitored emission from the first overtone of the C–H stretch region ($\approx$5900 cm^{-1}) through a 5525–6625 cm^{-1} bandpass filter. A one inch focal length sapphire lens was placed in front of this detector in order to collect more overtone emission, which had initial intensity $\approx$17 times weaker than the fundamental band emission for benzene-h_6, and $\approx$5 times weaker for benzene-d_6. Experiments with and without the lens showed that the measured collisional de-

cay rates were unaffected by the change in detector field of view induced by insertion of the lens (i.e., diffusion of excited molecules did not contribute significantly to the observed emission decays). The benzene-d_6 experiments were performed in a similar manner, using a 2100–2500 cm^{-1} bandpass filter for the C–D stretch fundamental band ($\approx$2290 cm^{-1}) and a 3600–5000 cm^{-1} filter for the first overtone ($\approx$4500 cm^{-1}).

Emission signals were amplified with a Tektronix AM 502 AC-coupled amplifier and averaged over 10000–30000 laser pulses (pulse repetition frequency $\approx$20 Hz, fluence $\leqslant$25 mJ/cm^2) for 21 separate benzene-h_6 and 14 benzene-d_6 experimental runs at pressures between 30 and 70 mTorr. Gas samples (benzene-h_6: Baker; benzene-d_6, 99.5 at% D: Sigma) were degassed prior to use and introduced into the cell through a fine-control needle valve. Constant pressure flowing conditions were employed in order to avoid any accumulation of photolysis products during experimental runs [12,13]. Pressures were maintained within $\pm$1 mTorr throughout each run as measured by a 1 Torr capacitance manometer (Baratron model 227).

3. Results

3.1. IRF calibrations

Experimental IRF decay curves for benzene-h_6 are shown in fig. 1, scaled to the same initial intensity. Time zero in fig. 1 is the time at which the laser is triggered. A delay of approximately one microsecond between the laser trigger and arrival of the laser pulse is followed by a several microsecond detector risetime and then decay of the emission due to collisional deactivation. The detector used to measure the overtone emission had a faster response time; in addition, a small amount of stray laser light contributed an initial spike to the first two microseconds of the overtone signals. In all cases, the spike disappeared within the risetime of the detector and did not affect the resulting measured decays. A small amount of thermal emission contributed to the lowest frequency band measured (the benzene-d_6 fundamental at 2290 cm^{-1}) at long times, and was eliminated by fitting the benzene-d_6 decays to a function which included a thermal emission term as part of the background (see below).

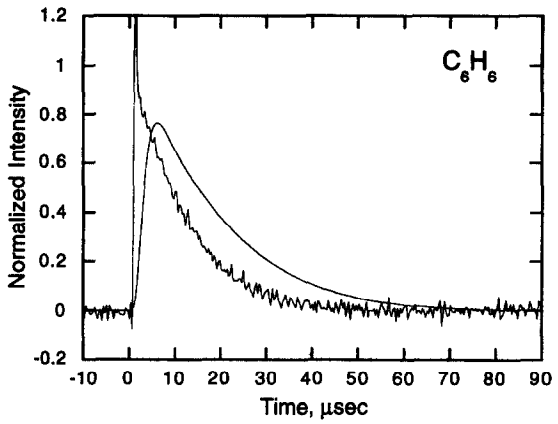

Fig. 1. Experimental IRF signals for benzene-h_6 (pressure=37 mTorr), normalized to unity. Upper curve: fundamental band. Lower curve: overtone band.

The measured IRF decays depend on the number of gas kinetic collisions experienced by the emitting molecules, such that when the timescales of runs performed at various pressures are converted to a collisional scale, background is subtracted, and initial intensities are normalized, the results form a single curve, as shown in fig. 2 for benzene-h_6. Lennard-Jones parameters used previously [11] were used to convert each run to a collision scale. For both the fundamental band and overtone emission, signal-averaged decays were compiled by combining all experimental runs and discarding all points affected by the detector response. Each such decay data set was then fitted using nonlinear least squares to a function of the form

$$\langle\langle I(N_c)\rangle\rangle = A\exp(-k^1N_c - b^1N_c^2) + B\,, \qquad (1)$$

where N_c is the average number of gas kinetic collisions undergone, and renormalized to $A=1$ and $B=0$. Due to the unavoidable effect of the detector response time, only experimental points up to $\langle\langle I(N_c)\rangle\rangle \approx 0.8$, corresponding to about four collisions, are included in the signal-averaged decay data set, and an extrapolation to $\langle\langle I(N_c\rangle\rangle = 1$ is required to determine the initial intensity at the excitation energy. Fitted parameters k^1 and b^1 for each of the four IRF bands measured are presented in table 1.

In fig. 1, it is evident that emission from the over-

Table 1
IRF decay parameters for benzene-h_6 and benzene-d_6

Molecule	C–H (C–D) stretch band	k^1	b^1
C_6H_6	fundamental	−0.0498 [a]	−0.000376 [a]
	first overtone	−0.0824 [a]	−0.00710 [a]
C_6D_6	fundamental	−0.0252 [b]	−0.000389 [b]
	first overtone	−0.0589 [a]	−0.000558 [a]

[a] From eq. (1). [b] From eq. (4).

tone band decays at a faster rate than the fundamental band emission. As the excited molecules are deactivated, the subset of excited molecules with sufficient quanta to emit in the C–H or C–D stretching mode (≥ 1 for fundamental band emission, ≥ 2 for overtone band emission) becomes depleted more rapidly for the overtone, leading to a faster IRF decay. The relative IRF intensities from the two bands in this way constitute a measure of the relative populations of the two emitting subsets, and can be used as a direct measure of the width of the overall energy population distribution.

For a given emission band i, the time-dependent total observed fluorescence can be expressed as

$$\langle\langle I(t)\rangle\rangle_i = \int_0^\infty f(t,E) I_i(E)\,\mathrm{d}E\,, \qquad (2)$$

where $f(t, E)$ is the energy population distribution function for excited molecules with vibrational energy E at time t, and $I_i(E)$ is the microcanonical emission intensity, which is unique for each band. The backbone of the IRF technique is the fundamental expression for $I_i(E)$ [15,1] which relates the observable quantity, IRF intensity, to the vibrational energy of the emitting molecules:

$$I_i(E) = [\rho_s(E)]^{-1} \sum_n^{v_{max}} A_i^{v,v-n} \rho_{s-1}(E-E_v)\,, \qquad (3)$$

where $A_i^{v,v-n}$ is the Einstein coefficient for spontaneous emission from level v to level $v-n$ in a given model ($n=1$ for a fundamental band, 2 for the first overtone), E_v is the total energy contained in the emitting mode ($=vh\nu$ for a harmonic oscillator), and $\rho_{s-1}(E-E_v)/\rho_s(E)$ is a density of states expression which describes the number of ways energy E can be distributed among all the vibrational modes such that the emitting mode contains the required energy E_v (see ref. [1] for a full discussion of the $I_i(E)$ expression, and references therein for experimental demonstrations of its validity). The Einstein coefficients $A^{v,v-n}$ for the various transitions observed in the experiments were calculated as described in the Appendix, according to the procedure in ref. [16].

$I_i(E)$ for C–H and C–D stretching mode fundamental and first overtone bands (hereafter denoted as I_1 for fundamental bands and I_2 for first overtones) was calculated using eq. (3) and exact count densities of states (Stein–Rabinovich method) [17]. Vibrational frequencies and diagonal anharmonicities were taken from ref. [18] for both benzene-h_6 and benzene-d_6, and only transitions with frequencies within the experimental bandpass filter transmittance ranges were included in the calculations.

3.2. Potential sources of systematic error

This experiment is dependent on the measurement of IRF from two well-defined, isolated bands which are assumed to be purely C–H (or C–D) stretch mode emission from all vibrational levels populated at the experimental energies. In the following, several possible sources of systematic error are described, along with our efforts to minimize their effects:

(1) *Contamination from non C–H (or C–D) stretch IRF.* The observed modes are well isolated from other identifiable bands in gas phase absorption spectra of the two molecules. For benzene-h_6, small contributions from several combination bands ($\nu_9+\nu_{18}$ at 2216 cm^{-1}, $\nu_9+\nu_{15}$ at 2328 cm^{-1}, $\nu_{10}+\nu_{19}$ at 2341 cm^{-1}, $\nu_3+\nu_{18}$ at 2405 cm^{-1}) [19] in the 2100–2500 cm^{-1} region were measured by using IRF observed through a narrow bandpass filter and then subtracted from the observed 2000–3300 cm^{-1} emission. A significant amount of underlying continuum emission in the benzene-h_6 C–H stretch fundamental region has been observed previously [20] (see fig. 11), but could not be measured for the overtone region, and has not been measured at all for benzene-d_6. The C–H stretch region continuum emission appears to decay more rapidly with collisional deactivation than the band itself, and could slightly distort the observed overall emission decay. In the absence of exact information about the contribution from continuum emission, we have assumed that it contributed roughly similar rel-

ative amounts to both the fundamental band and overtone emission, and have ignored it in our calculations. An independent measurement based on the time- and wavelength-resolved C–H stretch region spectrum of benzene-h_6 is free of complications from non-C–H stretch emission, and is in reasonable agreement with the broadband emission results, indicating that the continuum emission does not play an important role.

(2) *Contamination from thermal emission.* A small emission component at long timescales has been observed only in the benzene-d_6 C–D stretch fundamental region signal, and can be attributed to thermal emission due to the ≈ 50 K temperature rise following laser excitation. This component was eliminated by fitting the observed signals to eq. (1) including a term incorporating the temperature rise and resulting thermal emission:

$$\ll I(t) \gg_1 = A \exp(-k_1^1 t - b_1^1 t^2) + A_{\text{th}} \exp\{-h\nu[kT(t)]^{-1}\} + C, \quad (4)$$

$$T(t) = T_0 + (N^*/N) \exp(-B_{\text{th}} t) \times [E_0 - E(t)](C_v)^{-1}, \quad (5)$$

The three terms in eq. (4) represent non-thermal and thermal emission from excited molecules, plus background signal (measured at long times). The temperature rise following excitation was described by eq. (5), where T_0 and E_0 are the initial temperature (300 K) and excitation energy (40900 cm^{-1}), N^*/N is the fraction of excited molecules (≈ 0.005), $E(t)$ roughly describes the vibrational energy decay due to collisional energy transfer, C_v is the molecular heat capacity, and A_{th} and B_{th} (which is related to thermal conductivity) are fitted parameters. $T(t)$ determined this way rises to about 350 K, in agreement with an estimate based on the heat capacity and number of excited molecules produced with the experimental laser fluences. Thermal emission was not observed to contribute significantly to the higher frequency overtone and benzene-h_6 fundamental signals.

(3) *Filter cut-off of transitions from higher vibrational levels.* Bandpass filters used for the benzene-h_6 overtone and benzene-d_6 fundamental bands cut off a small amount of emission from transitions originating in $v=4$ and higher levels. For benzene-h_6, the diagonal anharmonicity and slight energy dependence of $\Delta v = -1$ transitions has been measured [20], allowing a precise estimation of the frequencies of $\Delta v = -2$ transitions. The $4 \rightarrow 2$ and higher transitions are calculated to lie almost entirely outside the filter transmission window, and were neglected in all calculations. For benzene-d_6, $\Delta v = -1$ transitions from $v=4$ and higher were neglected for similar reasons.

(4) *Extrapolation of* $\ll I(t) \gg_t$ *to* $t=0$. Due to the finite time response of the infrared detectors, only emission after about 5 μs (about four collisions at the experimental pressures) could be measured, and an extrapolation to $t=0$ using eq. (1) was necessary. Since eq. (1) was used to fit both the fundamental and overtone band decays, any systematic extrapolation error is likely to mostly cancel when the two decays are plotted against one another.

3.3. Population distribution widths and moments

Using the calculated $I_i(E)$ for each band in eq. (2) above results in two equations, each containing $f(t, E)$. In order to extract information about $f(t, E)$ from the experimental data, we have used two different approaches, referred to here as "parameter analysis" and "partial moments analysis". The first approach is more intuitive, based on conventional wisdom about the form of $f(t, E)$, while the second is more general and model-independent.

Parameter analysis. The parameter analysis approach assumes a form for $f(t, E)$ which can be characterized by a number of parameters equal to the number of independent IRF band measurements (two in the case of two-color IRF). In the absence of information about the distribution function, and for a function where only two moments are known a Gaussian form is conventionally assumed [21]:

$$f(t, E) = [\sigma(t)]^{-1} \times \exp\{-[E - E_{\text{mc}}(t)]^2 / 2[\sigma(t)]^2\}, \quad (6)$$

where $E_{\text{mc}}(t)$ is the microcanonical energy such that $I(E_{\text{mc}}(t)) = \ll I(t) \gg$. A Gaussian form is convenient and appropriate for two reasons: (1) it provides a simple, well-defined parameter σ to describe the width of $f(t, E)$, and (2) Gaussian $f(t, E)$'s have been shown to result from master equation models using an exponential form for the collisional step-size function $P_c(E', E)$, an empirical form which empha-

sizes weak collisions [22]. Such models predict that larger values for $\langle \Delta E \rangle$, the average energy transferred per collision, will result in broader $f(t, E)$'s. As the width parameter σ increases, plots of $\langle\langle I(t) \rangle\rangle_1$ (the fundamental band) and $\langle\langle I(t) \rangle\rangle_2$ (the first overtone band) versus E_{mc} change systematically as shown in fig. 3 , inducing changes in the ratio $\langle\langle I(t) \rangle\rangle_2 / \langle\langle I(t) \rangle\rangle_1$ at all times t. This ratio can then be compared directly to experimental measurements of $\langle\langle I(t) \rangle\rangle_1$ and $\langle\langle I(t) \rangle\rangle_2$, and provides a direct measurement of σ over most of the deactivation.

Figs. 4 and 5 show the experimental $\langle\langle I(t) \rangle\rangle_2$ plotted against $\langle\langle I(t) \rangle\rangle_1$ for benzene-h_6 and benzene-d_6, respectively, compared to results calculated from eq. (2) using various values for the width σ in the $f(t, E)$ expression. In the experiments, the actual $f(t, E)$ is constrained to be a near δ-function at $t=0$, since the initial energy distribution produced by laser excitation of the initial 300 K thermal distribution is very narrow. Initial intensities plotted in figs. 4 and 5 are normalized to unity at $t=0$, $E_0=40700$ cm^{-1} (benzene-h_6) and 40900 cm^{-1} (benzene-d_6). The microcanonical ($\sigma=0$) curves are also normalized to

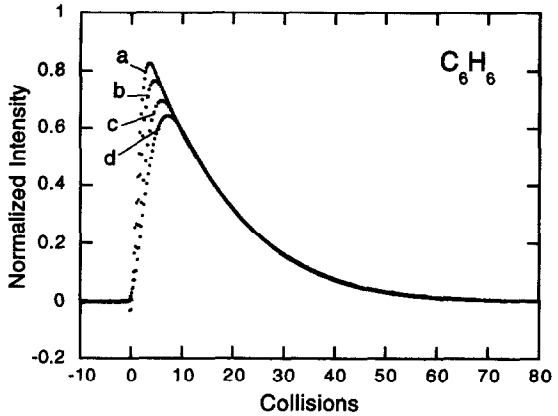

Fig. 2. Benzene-h_6 fundamental band normalized signal intensities versus average number of gas kinetic collisions at various pressures. (a) 29 mTorr. (b) 37 mTorr. (c) 52 mTorr. (d) 67 mTorr.

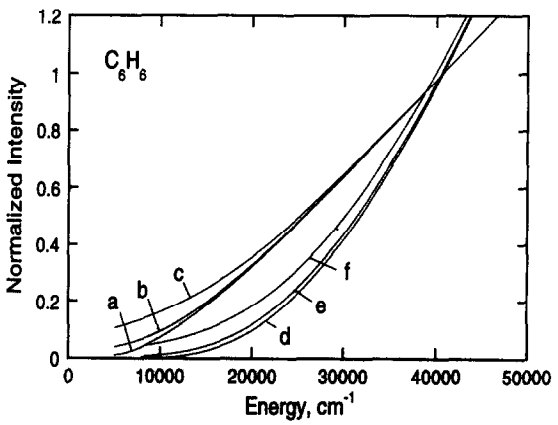

Fig. 3. Intensities $\langle I_i(E_{mc}) \rangle$ versus energies E_{mc} calculated from eqs. (2) and (4) with various values of σ^2 for benzene-h_6 fundamental and overtone bands. (a)–(c) fundamental band, $\sigma^2=0$, 1.8×10^7, 7.2×10^7 cm^{-1}; (d)–(f) overtone band, $\sigma^2=0$, 1.8×10^7, 7.2×10^7 cm^{-2}.

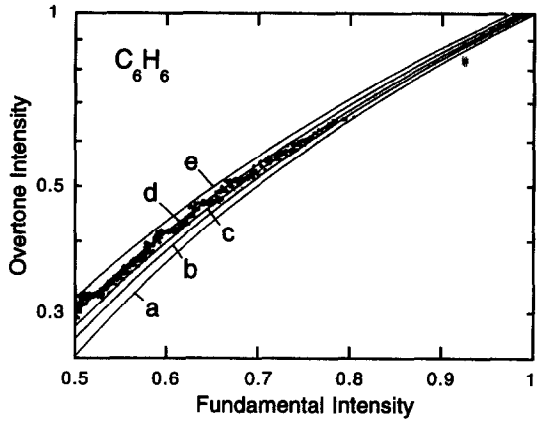

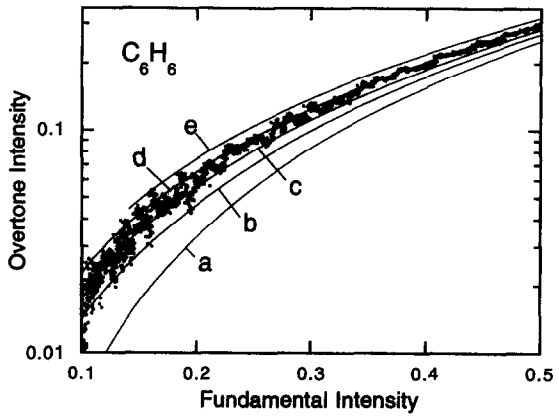

Fig. 4. Benzene-h_6 overtone band versus fundamental band intensity. Points: experimental. Lines: calculated from eqs. (2) and (4) using various σ^2 values. (a) $\sigma^2=0$ (microcanonical). (b) $\sigma^2=1.8\times10^7$ cm^{-2}; (c) $\sigma^2=3.2\times10^7$ cm^{-2}; (d) $\sigma^2=5.0\times10^7$ cm^{-2}; (e) $\sigma^2=7.2\times10^7$ cm^{-2}.

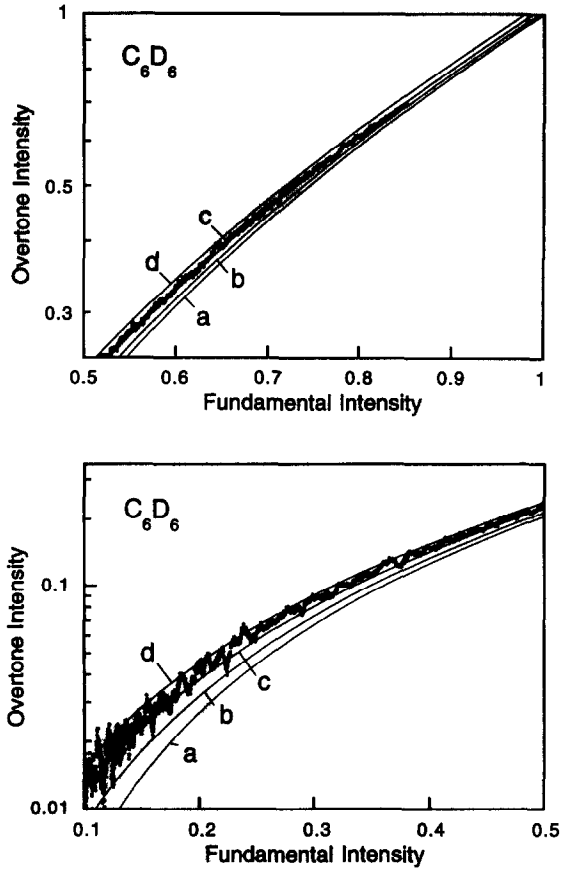

Fig. 5. Benzene-d_6 overtone band versus fundamental band intensity. Points: experimental. Lines: calculated from eqs. (2) and (4) using various σ^2 values. (a) $\sigma^2=0$ (microcanonical); (b) $\sigma^2=0.8\times10^7$ cm^{-2}; (c) $\sigma^2=1.8\times10^7$ cm^{-2}; (d) $\sigma^2=3.2\times10^7$ cm^{-2}.

unity at $t=0$, since the initial $f(t, E)$ is near-microcanonical. At lower energies, $f(t, E)$ differs significantly from a microcanonical δ-function and the width parameter σ required to match the experimental curves increases to a broad maximum ($\approx$7000 cm^{-1} for benzene-h_6, 5000 cm^{-1} for benzene-d_6) before narrowing again due to the $E=0$ lower integration limit in eq. (2) (see fig. 6). Ultimately, $f(t, E)$ must return to a room temperature thermal distribution. The larger widths measured for benzene-h_6 compared to benzene-d_6 agree with the exponential model prediction that more efficient collisions will broaden the distribution, since $\langle\Delta E\rangle$ is roughly 50% larger for benzene-h_6 [14].

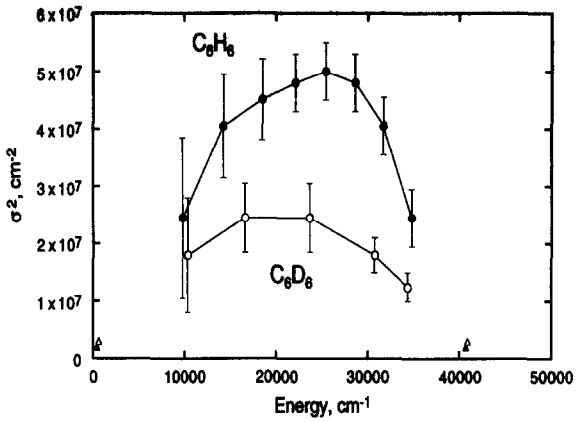

Fig. 6. σ^2 versus energy as determined by inspection of figs. 4 and 5. Triangles at $E=400$, 600, 40700, and 40900 cm^{-1} represent 300 K thermal distribution variances. Errors are estimated from figs. 4 and 5.

Partial moments analysis. The partial moments analysis approach makes no assumptions about the form of $f(t, E)$, and thus is of more general utility in extracting more detailed information about the energy population distribution. For an arbitrary $f(t, E)$, the nth moment is given by

$$M_n(t)=\int_0^\infty E^n f(t, E)\,\mathrm{d}E\,. \tag{7}$$

In IRF experiments, only excited molecules with sufficient energy to undergo the observed transitions contribute to the measured emission signals. Therefore, only the portion of $f(t, E)$ above a threshold energy E_0 ($=h\nu$ for a transition to $v=0$) contributes to the signal, and the form analogous to eq. (7) is

$$m_n(t)=\int_{E_0}^\infty E^n f(t, E)\,\mathrm{d}E\,, \tag{8}$$

where the $m_n(t)$ values represent the "upper partial moments" of $f(t, E)$ and are equal to the corresponding "full" moments $M_n(t)$ in the limit $f(t, E)=0$ for $E\leqslant E_0$. Master equation simulations, in which $f(t, E)$ is calculated using an assumed form for the collisional energy transfer step size distribution $P_c(E', E)$, can be used to assess the differences between $m_n(t)$ and $M_n(t)$ at times when a significant part of $f(t, E)$ lies below E_0.

If $I_i(E)$ in eq. (2) is expressed as a polynomial of order n, such that

$$I_i(E)=\sum_n C_{in}E^n \quad (E\geqslant E_0)\,, \tag{9}$$

then eq. (2) becomes

$$\langle\langle I(t)\rangle\rangle_i=\sum_n C_{in}m_n(t)\,, \tag{10}$$

$$=\sum_n C_{in}M_n(t) \quad \text{when } f(t,E)=0 \text{ for } E\leqslant E_0\,. \tag{11}$$

Measurement of $\langle\langle I(t)\rangle\rangle_i$ for n emission bands, each with a unique $I_i(E)$ dependence such that the coefficients C_{in} are different for each band, results in n equations in n unknowns and allows up to n upper partial moments $m_n(t)$ to be determined. This approach potentially can be applied to any experimental technique in which multiple processes with unique energy dependences are observed, including time- and wavelength-resolved ultraviolet absorption. Figs. 7 and 8 show results of the partial moments analysis for benzene and benzene-d_6, where independent measurement of two emission bands for each molecule yields the first two upper partial moments $m_1(t)$ and $m_2(t)$ at each time increment. To facilitate comparison with the parameter analysis results, figs. 7 and 8 show the variance σ^2, defined as

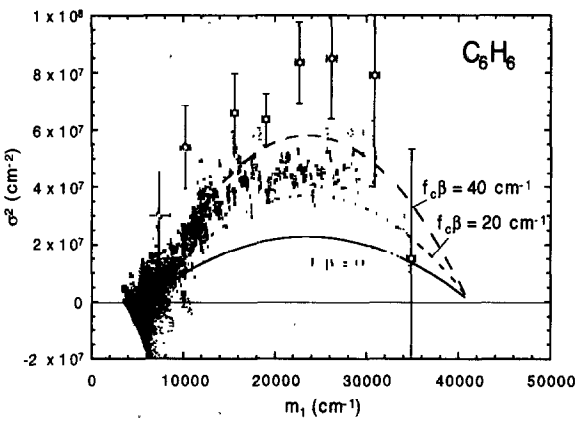

Fig. 7. Variance versus $m_1(t)$ for benzene-h_6, calculated by partial moments analysis. Points: experimental two-color broadband results; circles: experimental wavelength-resolved results; solid line: exponential model for $P_c(E', E)$; dashed lines: bi-exponential model for $P_c(E', E)$: $f_c\beta=20\ \text{cm}^{-1}$ (short dashes) and $f_c\beta=40\ \text{cm}^{-1}$ (longer dashes).

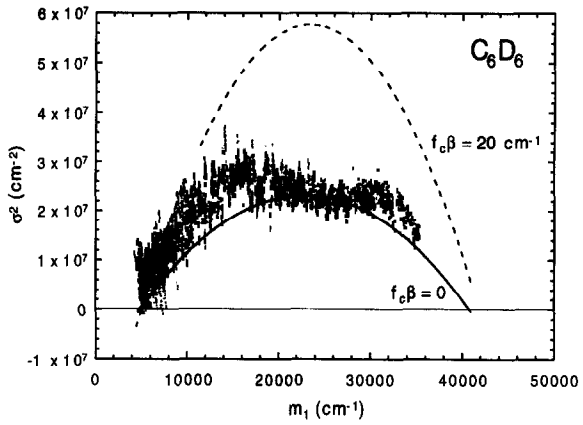

Fig. 8. Variance versus $m_1(t)$ for benzene-d_6, calculated by partial moments analysis. Points: experimental two-color broadband results; solid line: exponential model for $P_c(E', E)$; dashed line: bi-exponential model, $f_c\beta=20\ \text{cm}^{-1}$.

$$\sigma^2=m_2-(m_1)^2 \tag{12}$$

plotted versus $m_1(t)$. Rough agreement with the results in fig. 6, in which Gaussian forms for $f(t, E)$ were assumed, indicates that the population distributions are approximately described by Gaussians, especially in the case of benzene-d_6.

In eq. (9), $I_i(E)$ is approximated by a polynomial of order n equal to the number of independent emission band measurements available. For low values of n (e.g. $n=2$ in two-color experiments), this approximation introduces a significant amount of error into the results for partial moments analysis. Improved polynomial fits to $I_i(E)$ can be obtained by dividing the energy range into overlapping segments and fitting $I_i(E)$ for each segment independently; however, the width of each such segment must be large compared to the width of the population distribution $f(t, E)$, such that contributions to $I_i(E)$ from population outside the segment range are negligible. Fits of segments of width 20000 cm^{-1} have been found to improve the overall quadratic fit of $I_i(E)$ markedly, while minimizing errors due to narrowing of the energy range. Such deviations have been analyzed in detail for simulated data sets, and are discussed in the following section.

3.4. Master equation simulations

The time-dependent population distribution $f(t, E)$ is closely related to $P_c(E', E)$, the collisional energy transfer step size distribution function. Using a stochastic master equation program developed to describe deactivation processes in highly excited molecules [23,24], we have simulated the experimental results using various guesses for the form of $P_c(E', E)$. Successful forms must reproduce simultaneously both the $\langle\langle I(t)\rangle\rangle_1$ and $\langle\langle I(t)\rangle\rangle_2$ experimental decays. Using the partial moments analysis approach described above, calculated moments and variances from the simulation results can be compared directly to values calculated from the experimental data.

We have considered three differential functional forms for $P_c(E', E)$ in the master equation simulations:

(1) *Microcanonical.*

$$P_c(E', E) = \delta(\langle\langle -\Delta E(E)\rangle\rangle), \tag{13}$$

$\langle\langle -\Delta E(E)\rangle\rangle$ is the bulk average energy transferred per collision. This form maintains a δ-function population $f(t, E)$ throughout the deactivation.

(2) *Exponential.*

$$P_c(E', E) \propto \exp[-(E-E')/\alpha(E)], \quad 0 \leqslant E' \leqslant E. \tag{14a}$$

$\alpha(E)$ is a parameter related to $\langle \Delta E(E)\rangle_d$, the average energy transferred in down steps starting at energy E, by

$$\langle \Delta E(E)\rangle_d = \alpha(E)\{1-\exp[-E/\alpha(E)]\}. \tag{14b}$$

This form favors small step sizes and has been the standard one used to describe weak collisions [3,4,22]. It produces near-Gaussian population distributions [22] at all energies subject to the constraints $f(t, E) = f(t, E)_{\text{thermal}}$ at $t=\infty$ and $f(t, E) = f(t, E)_{\text{initial}}$ at $t=0$.

(3) *Bi-exponential.*

$$P_c(E', E) \propto (1-f_c)\exp[-(E-E')/\alpha(E)] + f_c \exp[-(E-E')/\beta(E)], \quad 0 \leqslant E' \leqslant E, \tag{15a}$$

where $\alpha(E)$ and $\beta(E)$ are parameters related to $\langle \Delta E(E)\rangle_d$ by

$$\langle \Delta E(E)\rangle_d = (1-f_c)\alpha(E)\{1-\exp[-E/\alpha(E)]\} + f_c\beta(E)\{1-\exp[-E/\beta(E)]\}. \tag{15b}$$

The bi-exponential model incorporates a small fraction f_c of "super-collisions" which transfer a large amount of energy, and has been used to model experimental results [6–10] as well as trajectory calculations [25,26]. This model produces population distributions which are near-Gaussian, yet have an enhanced low energy tail corresponding to rapid deactivation by large step-size collisions. The low energy tail has the effect of broadening (i.e. increasing the second moment of) the population distribution $f(t, E)$.

For all $P_c(E', E)$ models, normalization and calculation of collisional up-step probabilities were carried out as described previously [20,24,27]. The parameter $\alpha(E)$ was expressed in the form $C_1 + C_2E + C_3E^2$, with the coefficients adjusted in each simulation in order to obtain agreement with the experimental $\langle\langle I(t)\rangle\rangle_1$ decay. $\beta(E)$ was a constant equal to 20000 cm^{-1} in all bi-exponential model simulations. In fig. 10, population distributions $f(t, E)$ for the three models at a point midway through the simulated benzene-h_6 deactivation are shown. $\alpha(E)$ has been adjusted in each simulation so that the experimental $\langle\langle I(t)\rangle\rangle_1$ decay is reproduced; thus, the three distributions shown all produce the same fundamental band emission intensity as calculated from eq. (2), even though the average energy of each distribution varies due to the differences in $\alpha(E)$. The best fit $\alpha(E)$ for each step size model is listed in table 2, along with values derived from previous experiments for benzene-h_6 and benzene-d_6. Previous analyses [14] did not include the effects of the population distribution width in determining appropriate values for $\alpha(E)$ and $\beta(E)$.

Fig. 9 shows the variance, σ^2, as a function of the first moment of $f(t, E)$ for benzene, calculated for the exponential and bi-exponential models for $P_c(E', E)$. This figure indicates the magnitude of the errors involved in the quadratic approximation of $I_i(E)$ (eq. (9)), as well as the difference between "upper partial moments" and "full" moments as described above. In each panel of fig. 9, thick lines represent the exact "full" (solid line) and "upper partial" (dashed line) moments, calculated from the population distribu-

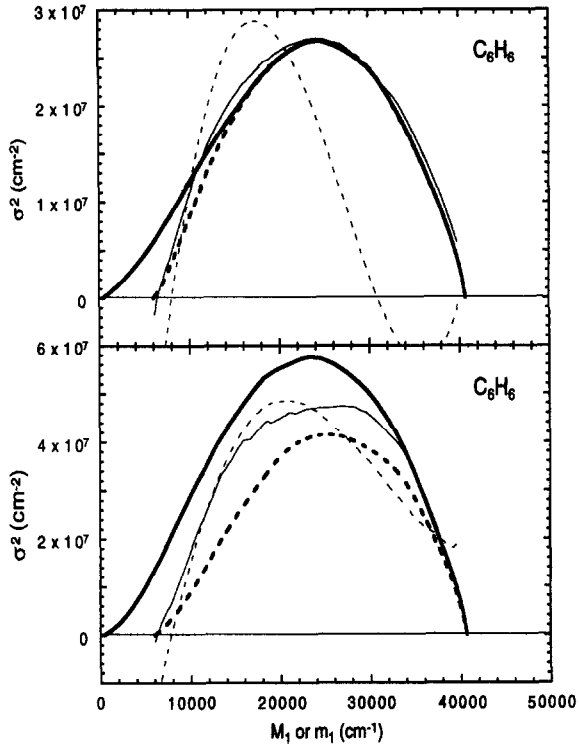

Fig. 9. Variance versus first moment for $P_c(E', E)$ models described in the text for benzene-h_6. Upper panel: exponential model; lower panel: bi-exponential model, $f_c\beta = 40\ cm^{-1}$. Thick solid lines: "full" moments; thick dashed lines: "upper partial moments"; thin dashed lines: from quadratic approximation to $I_i(E)$ over full energy range; thin solid lines: from quadratic approximation to $I_i(E)$ over segmented ranges (width of ranges = 20000 cm^{-1}).

tions produced from the simulations (e.g. the distributions shown in fig. 10). Fig. 9 shows that the upper partial moments deviate from the full moments only at low energies for the exponential model (upper panel), and at higher energies for a bi-exponential model ($f_c\beta = 40\ cm^{-1}$, lower panel). The deviation is due to the presence of significant population below the threshold for emission (6000 cm^{-1}), which occurs much earlier in the deactivation for the bi-exponential model (see fig. 10).

As discussed above, polynomial approximation of $I_i(E)$ according to eq. (9) introduces significant error to the partial moments analysis, especially in two-color experiments. Analysis of master equation simulations can be used to indicate the magnitude of this error for various models. In fig. 9, thin lines in each

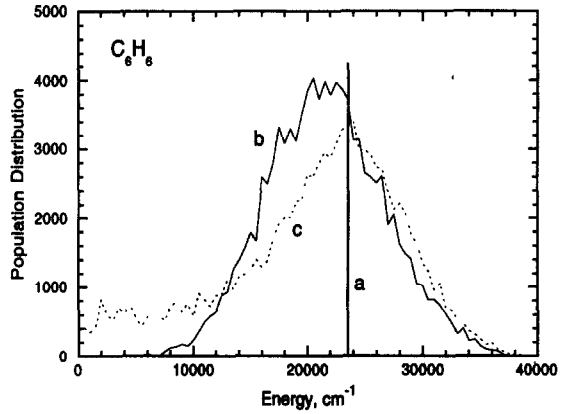

Fig. 10. $f(t, E)$ at $t = 30\ \mu s$ for three $P_c(E', E)$ models described in the text for benzene-h_6. (a) Microcanonical; (b) exponential; (c) bi-exponential, $f_c\beta = 40\ cm^{-1}$.

panel show upper partial moments calculated both from fitting $I_i(E)$ over the full energy range (dashed lines) and for overlapping 20000 cm^{-1} ranges (solid lines). The first method results in deviations from the exact upper partial moments due to relatively poor quadratic fits, while the second method is subject to error when $f(t, E)$ is wider than 20000 cm^{-1}. For an exponential model (upper panel), $f(t, E)$ is never much wider than 20000 cm^{-1}, and the segmented fitting method accurately reproduces the exact upper partial moments. (Imperfections in the fits at low energies cause the non-physical negative variances shown). For a bi-exponential model (lower panel), $f(t, E)$ is wider and segmented fitting overestimates the exact upper partial moments by a small amount; however, the magnitude of this error in σ^2 is small compared to the differences between models, so that comparison to the experimental results can readily distinguish among different models for $P_c(E', E)$.

3.5. Comparison to two-color broadband emission

While $\alpha(E)$ and $\beta(E)$ can be adjusted in any master equation simulation to reproduce the experimental $\langle\langle I(t)\rangle\rangle_1$ decays at single wavelengths, simulations using different step size models show varying degrees of success in simultaneously reproducing multiple experimental $\langle\langle I(t)\rangle\rangle_i$ decays. This fact provides a means of discriminating between assumed forms of $P_c(E', E)$. Figs. 7 and 8 show σ^2 ver-

Table 2
Best fit $\alpha(E)$ parameters for various forms of $P_c(E', E)$

Molecule	$P_c(E', E)$ model	$\alpha(E)$ [a]		
		C_1 (cm^{-1})	C_2 ($\times 10^7$)	C_3 ($1/cm^{-1}$)
C_6H_6	exponential [b] (ref. [14])	41.5	0.0539	−4.85
	exponential [b]	79.6	0.0430	−1.32
	exponential [c]	82.0	0.0443	−1.36
	bi-exponential ($f_c\beta$=40 cm^{-1}) [c]	35.2	0.0383	−1.18
C_6D_6	exponential [b] (ref. [14])	61.3	0.0452	−6.60
	exponential [b]	81.0	0.0457	−5.15
	exponential [c]	86.1	0.0486	−5.48

[a] $\langle \Delta E(E) \rangle_d = C_1 + C_2 E + C_3 E^2$.
[b] Estimated from microcanonical calibration curves.
[c] Adjusted to fit experimental $\langle\langle I(t) \rangle\rangle_1$ decays.

sus m_1 calculated from partial moments analysis for the exponential and bi-exponential models compared to the two-color broadband experimental results. In each case, $I_i(t=0)$ has been normalized to unity and $\alpha(E)$ has been adjusted to obtain a close match to the experimental $\langle\langle I(t) \rangle\rangle_1$ decay. It is clear that a substantial deviation from the microcanonical model ($\sigma^2=0$) exists for both benzene-h_6 and benzene-d_6, due to the finite widths of the population distributions. The widths introduced by the exponential model produce closer agreement with the experimental curve for benzene-h_6, and nearly exact agreement for benzene-d_6 over much of the energy range. At low energies, noise in the experimental data results in non-physical negative variances.

For both molecules the best agreement is obtained by using a bi-exponential model which significantly changes the shape of $f(t, E)$ (see fig. 10). Fig. 7 includes bi-exponential model simulations involving various fractions f_c of "super-collisions". In these simulations, the super-collision step size parameter $\beta(E)$ was assumed arbitrarily to be 20000 cm^{-1}, and independent of E. For β larger than roughly $10\langle \Delta E(E) \rangle_d$ ($\approx$10000 cm^{-1} for benzene-h_6), simulations where the product $f_c\beta$ is a constant produce identical results (i.e., the simulations are only sensitive to the fraction of energy transferred in super-collisions). Figs. 7 and 8 show that $f_c\beta \approx 30 \pm 10$ cm^{-1} most closely matches the two-color broadband experimental data for benzene-h_6, while $f_c\beta \approx 5 \pm 5$ cm^{-1} provides the best fit for benzene-d_6.

3.6. Comparison to time- and wavelength-resolved $\Delta v = -1$ emission

A time- and wavelength-resolved C–H stretch region emission spectrum for benzene-h_6 [20] provides a second, independent means of measuring $f(t, E)$ during collisional deactivation. Shown in fig. 11, this spectrum partially resolves individual $\Delta v = -1$ C–H stretch transitions originating in $v=1$, 2, and 3, measured as a function of time. Gaussian curve fits of the spectrum yield relative intensities of the individual $\Delta v = -1$ components, which agree at $t=0$ (E=40700 cm^{-1}) with those predicted from eq. (3) within about 5%. Since individual transitions, rather than entire bands, are measured in this experiment, continuum emission and other non-C–H stretch emissions cannot interfere with the results (as is possible in the broadband measurements). A plot of $\langle\langle I(t) \rangle\rangle_{2\to1}$ versus $\langle\langle I(t) \rangle\rangle_{1\to0}$ yields similar information about $f(t, E)$ and can also be compared to master equation simulations using various models for $P_c(E', E)$. Fig. 7 includes partial moments analysis results of such a comparison to the two-color broadband experimental results, and to master equation model simulations. Best agreement with the wavelength-resolved results is obtained using a bi-exponential model with $f_c\beta$ on the order of 40–60 cm^{-1}.

4. Conclusions

Simultaneous measurement of IRF from two bands

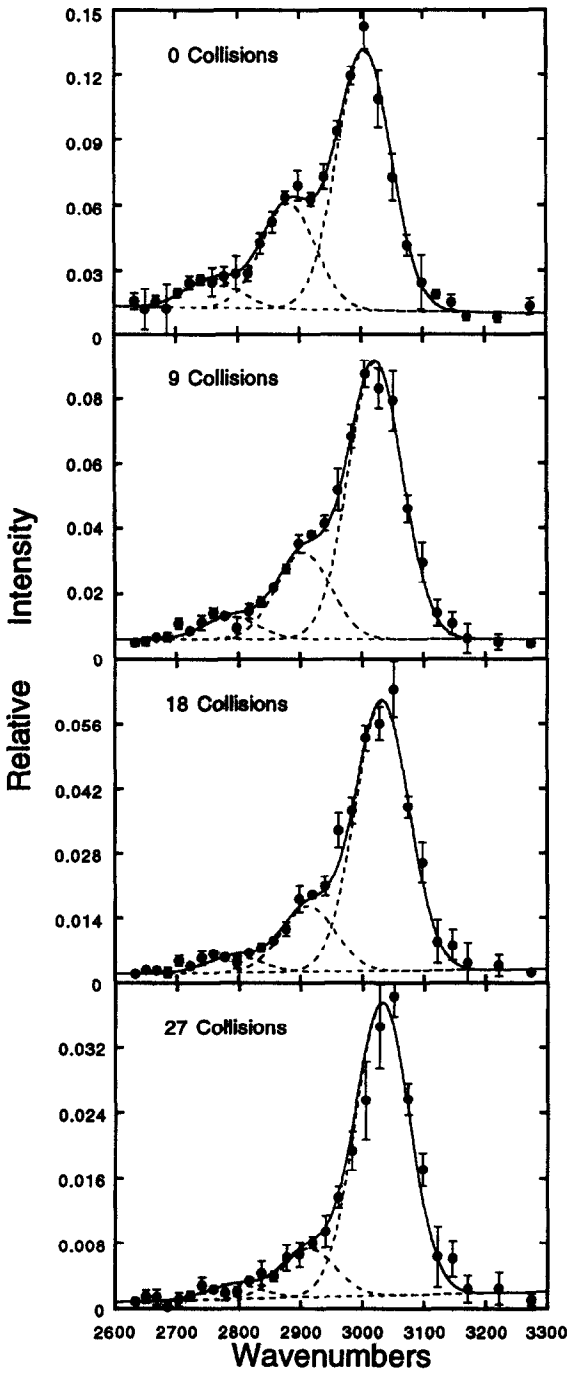

Fig. 11. C–H stretch region emission spectrum for benzene-h_6 following 248 nm laser excitation, $\approx 30\ cm^{-1}$ resolution. Panels show the spectrum following the indicated average number of collisions. Dashed lines show Gaussian lineshape fits to $1 \rightarrow 0$ ($\approx 3010\ cm^{-1}$), $2 \rightarrow 1$ ($\approx 2890\ cm^{-1}$), and $3 \rightarrow 2$ ($\approx 2770\ cm^{-1}$) components. The solid line is a sum over the three components plus a background (continuum) term.

of widely separated frequencies has been used to measure quantities related to the means and variances, or first two moments, of the excited molecule population distribution during a substantial portion of the collisional deactivation of highly vibrationally excited benzene-h_6 and benzene-d_6. The derived energy population distributions differ markedly from a microcanonical δ-function, and agree well for both molecules with those predicted by the widely used but purely empirical exponential form for the collisional energy transfer step size distribution function. Modifications to the exponential step size function to include a small "super-collision" component appear to improve the fit to the experimental measurements for both molecules. A generalized data analysis method for deriving information about higher moments of the energy population distribution from multiple emission band measurements of IRF hold promise for improving the utility of the IRF, as well as other techniques in energy transfer studies. Future investigations are planned with benzene-h_6 involving multi-color IRF, and including deactivation by other collider molecules.

Acknowledgement

This work was funded in part by the Department of Energy, Office of Basic Energy Sciences. JDB thanks NASA for partial support through a Graduate Student Researchers Program Fellowship.

Appendix

Einstein coefficients $A^{v,v-n}$ for various transitions $v \rightarrow v-n$ were calculated according to ref. [16]. For a transition involving a single mode, the transition moment matrix element is given by the following expressions for one-quantum transitions ($|\Delta v| = 1$):

$$\langle v|\mu|v+1\rangle = k_1[(v+1)/2]^{1/2}; \qquad (A.1)$$

for two-quantum transitions ($|\Delta v| = 2$):

$$\langle v|\mu|v+2\rangle = k_2[(v+1)/2]^{1/2}[(v+2)/2]^{1/2}; \qquad (A.2)$$

for any transition:

$$\langle v|\mu|v+n\rangle = k_n \prod_{n'=1}^{n} [(v+n')/2]^{1/2} . \quad \text{(A.3)}$$

Combination band matrix elements are given, in general, by

$$\langle v_a v_b|\mu|v_a+n, v_b+m\rangle = k_{nm} \prod_{n'=1}^{n} \prod_{m'=1}^{m} [(v_a+n')/2]^{1/2} \times [(v_b+m')/2]^{1/2} . \quad \text{(A.4)}$$

The k's in these equations contain the details of the transition moment operators and are independent of v. Einstein coefficients $A^{v,v-n}$ are proportional to the squares of the matrix elements, and to the cubes of the transition frequencies, such that

$$A^{v,v-1} = C_1 k_1^2 \{[(v-1)+1]/2\} (\nu_{v\to v-1})^3 = vA^{1,0} (\nu_{v\to v-1}/\nu_{1\to 0})^3 , \quad \text{(A.5)}$$

$$A^{v,v-2} = \tfrac{1}{2} v(v-1) A^{2,0} (\nu_{v\to v-2}/\nu_{2\to 0})^3 , \quad \text{(A.6)}$$

$$A^{v,v-n} = \frac{v!}{n!\,(v-n)!} A^{n,0} (\nu_{v\to v-n}/\nu_{n\to 0})^3 . \quad \text{(A.7)}$$

These three expressions were employed in eq. (3).

References

[1] J.R. Barker and B.M. Toselli, Intern. Rev. Phys. Chem. (1993), in press.

[2] H. Hippler and J. Troe, in: Bimolecular collisions, eds. J.E. Baggott and N. Ashfold (The Royal Society of Chemistry, London, 1989) p. 209.

[3] I. Oref and D.C. Tardy, Chem. Rev. 90 (1990) 1407.

[4] D.C. Tardy and B.S. Rabinovitch, Chem. Rev. 77 (1977) 369.

[5] M. Quack and J. Troe, in: Gas kinetics and energy transfer, Vol. 3, eds. P.G. Ashmore and R.J. Donovan, Specialist Periodical Reports (The Chemical Society, London, 1977) p. 175.

[6] H.G. Lohmannsroben and K. Luther, Chem. Phys. Letters 144 (1988) 473.

[7] K. Luther and K. Reihs, Ber. Bunsenges. Physik. Chem. 92 (1988) 442.

[8] K. Luther, private communciation (1990).

[9] S. Hassoon, I. Oref and C. Steel, J. Chem. Phys. 89 (1988) 1743.

[10] I.M. Morgulis, S. S. Sapers, C. Steel and I. Oref, J. Chem. Phys. 90 (1989) 923.

[11] H.S. Johnston, private communication (1992).

[12] M.L. Yerram, J.D. Brenner, K.D. King and J.R. Barker, J. Phys. Chem. 94 (1990) 6341.

[13] B.M. Toselli, J.D. Brenner, M.L. Yerram, W.E. Chin, K.D. King and J.R. Barker, J. Chem. Phys. 95 (1991) 176.

[14] B.M. Toselli and J.R. Barker, J. Chem. Phys. 97 (1992) 1809.

[15] J.F. Durana and J.D. McDonald, J. Chem. Phys. 64 (1976) 2518.

[16] C. Camy-Peyret and J.-M. Flaud, in: Molecular spectroscopy: modern research, Vol. 3, ed. K.N. Rao (Academic Press, New York, 1985) p. 69.

[17] S.E. Stein and B.S. Rabinovitch, J. Chem. Phys. 58 (1973) 2438.

[18] L. Goodman, A.G. Ozkabak and S.N. Thakur, J. Phys. Chem. 95 (1992) 9044.

[19] R.H. Page, R.H. Shen and Y.T. Lee, J. Chem. Phys. 88 (1988) 5362.

[20] J.D. Brenner and J.R. Barker, Astrophys. J. Letters 388 (1992) L39.

[21] R.S. Bevington and D.C. May Jr., Handbook of probability and statistics with tables, 2nd Ed. (McGraw-Hill, New York, 1979) p. 121.

[22] J. Troe, J. Chem. Phys. 77 (1982) 3485.

[23] J.R. Barker, Chem. Phys. 77 (1983) 201.

[24] J.R. Barker, J. Phys. Chem. 96 (1992) 7361.

[25] G. Lendvay and G.C. Schatz, J. Phys. Chem. 94 (1990) 8864.

[26] D.L. Clarke, K.C. Thompson and R.G. Gilbert, Chem. Phys. Letters 182 (1991) 357.

[27] J. Shi and J.R. Barker, Intern. J. Chem. Kinetics 22 (1990) 187.